Footprint reduction by angle-weighted stacking after migration

Joanna K. Cooper, Gary F. Margrave, and Don C. Lawton

ABSTRACT

In prestack migrated seismic data, acquisition footprint artefacts can manifest as residual migration wavefronts. Due to inadequate spatial sampling, the wavefronts do not properly interfere: constructively where reflectors exist and destructively elsewhere. Prestack migration algorithms have different ways of sorting, regularizing, and weighting the input data, which results in differing abilities to deal with poor sampling. Additional normalizations are performed on traces after migration but before stacking to form the final migrated image. In this paper, a weighting scheme in a Kirchhoff shot-record migration, which partially compensates for irregularities in the angle-dependent illumination of an image point, is described and assessed. Although the weights are applied in the context of migrating common-source gathers, the weights are dependent on the locations of all shots and receivers in a survey, and are applied to traces during the stacking process after migration; they are therefore not limited to the case of shot-record migrations. The weights are a function of image point location and delta, an angle describing the direction of the vector that bisects the opening angle formed by source-to-image-point and receiver-to-image-point rays. We compute hit counts at each image point for different delta bins and use these to compute weights that are applied to delta-limited Kirchhoff migrations. The zero delta hit-count is identical to traditional common midpoint fold and collectively these hit counts generalize the fold concept to prestack migration. The method, when applied to 2D model data shows potential for reducing footprint artefacts. The same type of weights can also be applied in the case of 3D data.

INTRODUCTION

Previously (Cooper et al., 2007), we described the initiation of a study of acquisition footprint in 2D and 3D seismic data. Acquisition footprint, an example of which is shown in Figure 1, generally consists of periodic amplitude variations that are unrelated to changes in elastic properties of the subsurface, but rather are artefacts of the choice of acquisition geometry and processing techniques. Footprint is often most obvious on time, depth, or horizon slices from 3D volumes, but the problem is also present in 2D data. The artefacts are observed to occur in many stages of processing, including stacked sections, poststack migrations, and prestack migrations. In our study, we take the approach that poor (i.e. sparse and irregular) sampling of the seismic wavefield is at the root of the footprint artefacts and therefore we numerically model seismic data recorded with ideal sampling. This ideal sampling corresponds to an acquisition geometry that we term "exhaustive", with dense grids of sources and receivers that allow for prestack seismic data that exhibit no spatial aliasing in either common source or common receiver gathers. By selectively removing traces from the exhaustive dataset, we form more sparsely sampled datasets that mimic more realistic field acquisition geometries. Processing of both the exhaustive and decimated datasets with various algorithms allows us to examine the effect of spatial sampling on footprint, and also to observe how algorithmic differences influence the footprint artefacts.
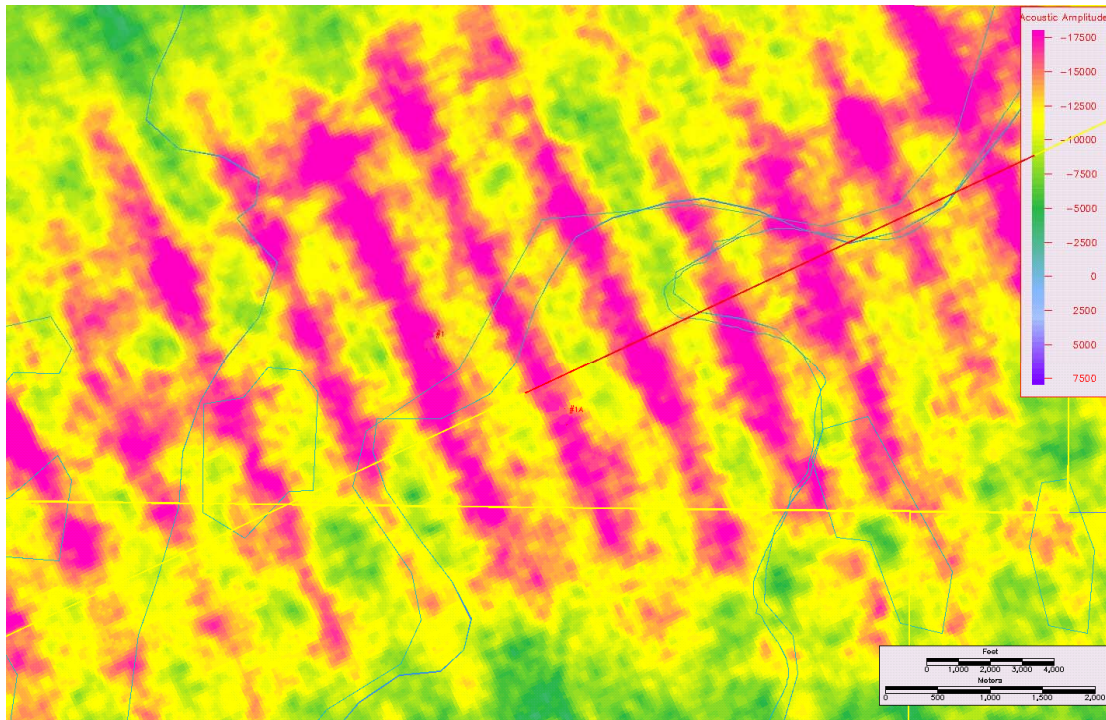
FIG. 1. Example of acquisition footprint consisting of periodic amplitude variations on a horizon slice from a 3D volume.

In this paper we focus on footprint after prestack migration and build on the 2D and 3D footprint simulations described by Cooper et al. (2007). The model for the 2D simulation was 400 m long, with a reflector located at 200 m depth. The reflector had a uniform positive reflection coefficient, except for a small opposite-polarity anomaly in the exact centre of the reflector. The exhaustive acquisition geometry involved sources and receivers located at 5 m increments from 0 m to 400 m, on a flat surface. All receivers were live for every shot. Five decimated datasets were produced by simulating larger shot intervals, of 10 m, 25 m, 50 m, 100 m, and 200 m. Figure 2 shows the results from prestack Kirchhoff migration of each dataset, followed by stacking of the migrated shot records, from Cooper et al. (2007). The migration algorithm uses weights derived by Bleistein et al. (2001), modified for variable velocity. With large shot intervals, footprint artefacts consisting of residual migration wavefronts appear in the images. At constant depth, the wavefronts are regularly spaced and if amplitudes were extracted along a depth slice that crossed those wavefronts, periodic amplitude variations (i.e. footprint) would be observed. As discussed in Cooper et al. (2007), we observed a correlation between the presence of the wavefronts in the final images and the presence of spatial aliasing in common receiver gathers, which indicated a possible link between spatial aliasing and footprint.
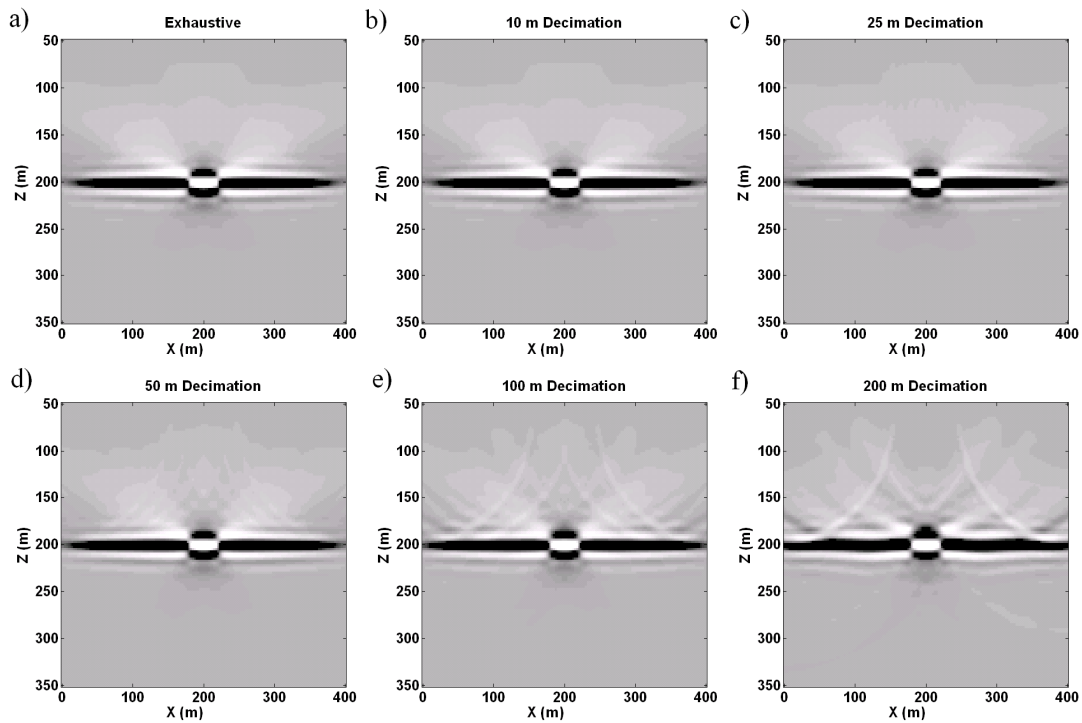
FIG. 2. Images produced from stacking migrated shot records from the exhaustive dataset and the five decimated datasets, from Cooper et al. (2007). The exhaustive dataset (a) had a shot spacing equal to the receiver spacing. The five decimated datasets had shot spacings of twice (b), five times (c), ten times (d), twenty times (e), and forty times (f) the receiver spacing. Footprint artefacts consisting of residual migration wavefronts are observable in d) through f) and are also subtly present in c).

Cary (2007a, 2007b) described a similar 2D footprint simulation which produced residual migration wavefronts after shot-record migrations. Using a common-offset migration algorithm also produced the same results; incomplete cancellation of migration wavefronts occurred when the shot spacing was not fine enough. However, applying partial NMO before migration to correct the offset of each trace to that of the centre of the offset bin was successful in reducing the presence of the footprint. In a different study, Cary (1999) showed the ability of partial stacking of common-offset gathers before migration to help overcome spatial aliasing associated with sparse sampling. In that paper, he commented on the ability of the technique to increase the fidelity of reflection waveforms of shallowly dipping events in the final migrated images, though the quality of steeply dipping events suffered when aliasing was severe. These studies suggest that regularization in the offset dimension is helpful in increasing the accuracy of reflection amplitudes and, perhaps in a related way, in reducing footprint artefacts. The work is also consistent with our ideas about the role of spatial aliasing in footprint; the reduction in the severity of spatial aliasing being achieved, in this case by imposing a model (i.e. horizontal reflectors) during partial NMO correction, is associated with the footprint reduction.

Cooper et al. (2007) also described the initiation of our 3D footprint simulation. In this case, the model was 400 m by 400 m in x and y, with three reflectors in depth. Two reflectors, at 100 m and 180 m, were featureless, meaning they had a constant reflection

coefficient, and the third, at 200 m, had a sinuous channel feature in it. The exhaustive survey consisted of shots and receivers on a 10 m grid, as shown in Figure 3 a). Figure 3 b) shows the decimated survey, which mimics an orthogonal survey design, with shots and receivers still spaced at 10 m but now located in shot lines parallel to the y axis and receiver lines parallel to the x axis. The line spacings were 80 m. All receivers were live for every shot. Obviously, these were not the only possible choices for the survey designs. For example, the source and receiver positions could have been staggered, other types of decimations could have been produced, and a moving receiver patch could have been incorporated. These changes to the survey designs fall under future work in our larger study of footprint; for this paper, we stayed with these two designs in order to be able to compare to the results shown in Cooper et al. (2007). Figure 4 shows the results of the Kirchhoff shot-record migrations from that paper, created using a 3D version of the same Bleistein-weighted migration algorithm used for the 2D simulations.
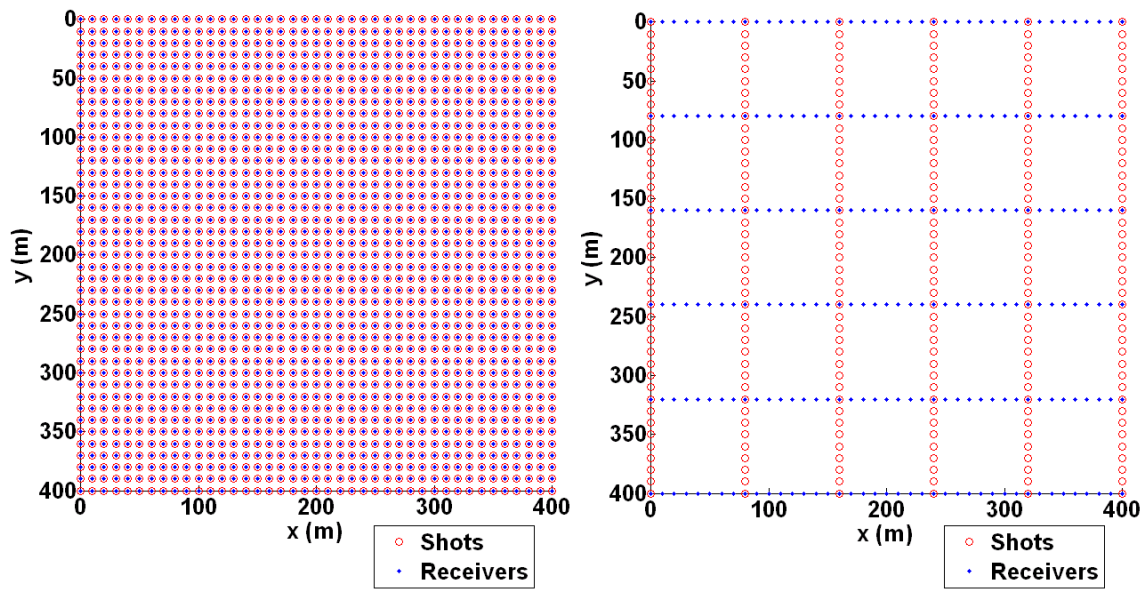

FIG. 3. Exhaustive (left) and decimated (right) survey geometries for 3D footprint simulations.

In comparing the migrations of the exhaustive and decimated datasets in Figure 4, periodic amplitude variations are observable in the decimated dataset, especially on the two featureless reflectors. Since those two reflectors are above the channel reflector, any residual migration wavefronts associated with the channel reflector would be crosscut by the slices at the two featureless reflectors, resulting in the observed footprint. The images of the reflector at 180 m contain an imprint of the channel, even though the reflection coefficient was constant at that level. This is due to wavelet sidelobes from the nearby channel reflection event; deconvolution was not applied to the data. The images from the exhaustive dataset do not show the periodic amplitude variations, but they do exhibit the same pronounced aperture imprint as in the decimated survey, with amplitudes decaying away from the middle of the survey.
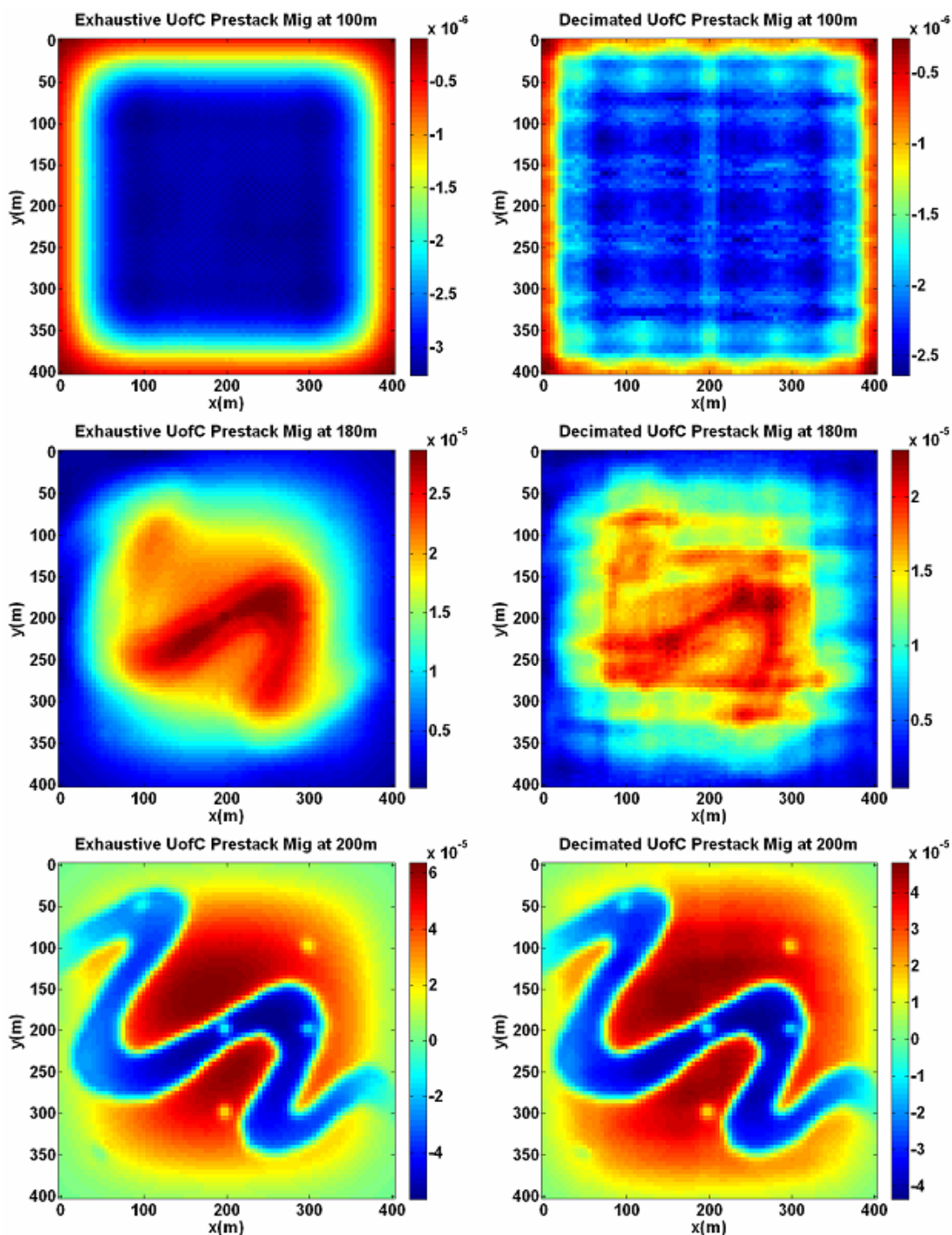
FIG. 4. Depth slices from prestack migrated volumes at the 100 m featureless reflector (top row), the 180 m featureless reflector (middle row), and the channel reflector (bottom row) from Cooper et al. (2007). Images in the left-hand column are from the exhaustive survey; those from the right-hand column are from the decimated survey.

Figure 5 shows two industrial prestack migrations of the same model, performed using common-offset and common-offset-vector migration algorithms (see Cooper et al. 2007 for more details). Comparison with Figure 4 shows that the industrial weighting schemes

result in images without the strong aperture imprints. They also show reduced footprint artefacts. For the purposes of this study, the most important observations from the comparison are that the offset-domain weighting seems to do a better job then our shot weights, and that the industrial empirical weights do a better job than our Bleistein theoretical weights. These observations motivated the present investigation, on achieving reduction in footprint by modifying the way traces are weighted in prestack migration. Of course, changing migration algorithms and weights is not the only way to attempt to reduce footprint. Among other things, improvement could result from regularization, in a manner similar to that observed in the 2D case; this could be accomplished perhaps by interpolation or partial stacking. At the extreme of partial stacking is full stacking, and simulations from Cooper et al. (2007) suggest that footprint in stacks and poststack migrations may not be as severe as after prestack migration. Here, though, we focus on benefits that can be achieved by attempting to weight prestack migrated traces to compensate for irregular angular illumination caused by poor sampling.
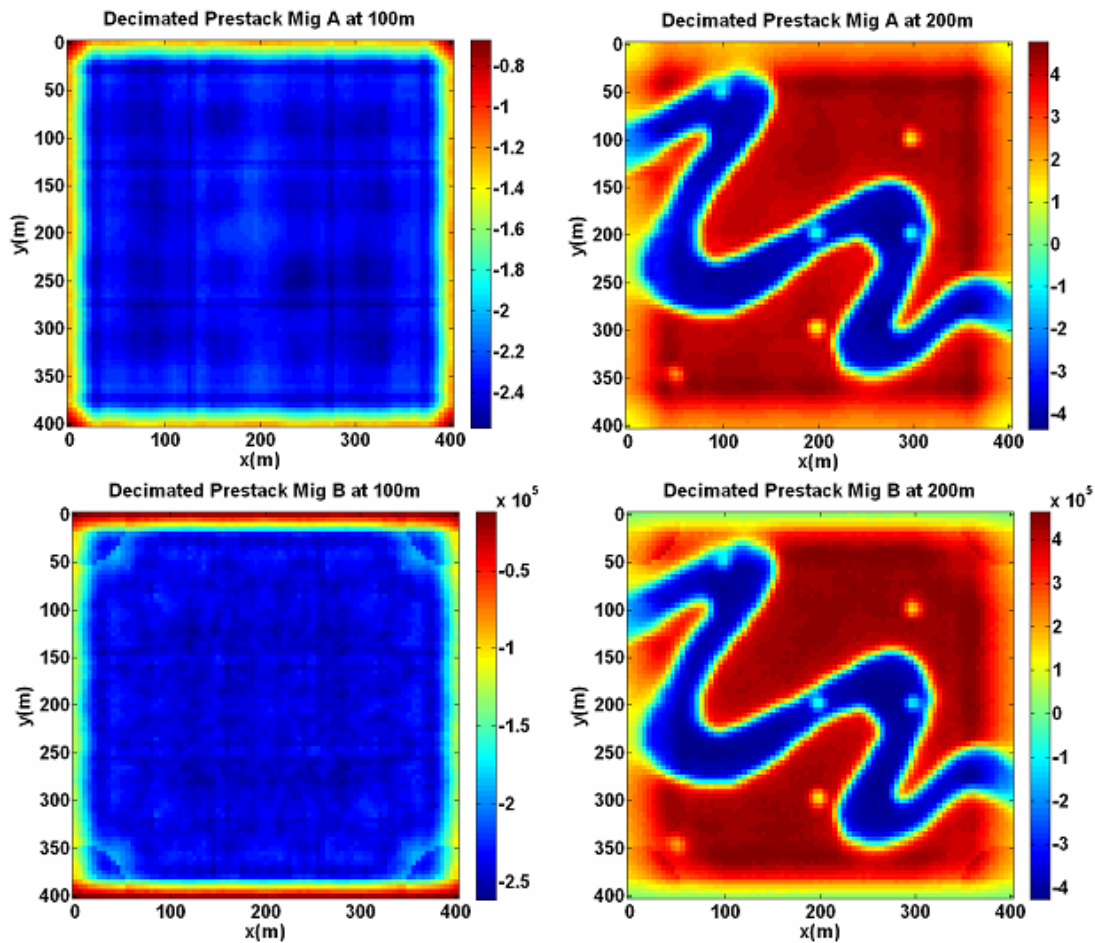

FIG. 5. Depth slices at 100 m (left) and 200 m (right) from prestack migrations of the decimated dataset performed using industry migration algorithms from Cooper et al. (2007). Comparison with Figure 4 shows the influence of migration algorithm on footprint.

METHOD

Different types of weighting in prestack migration produce many of the differences between algorithms. Weights can be applied to traces before migration, during migration, and after migration. With the observation in our 3D footprint simulations that different migration algorithms produced such different results, we began trying to improve the weighting in our Kirchhoff shot-record migration. We chose to stay with a shot-record migration, instead of moving to migrating other types of gathers such as common-offset gathers, because fundamentally in the absence of partial stacking before migration, the domain in which migration is implemented should not matter. With the Kirchhoff method, each trace could be migrated independently; it is only the weights that are applied to each trace that give rise to differences in the final image. As discussed by Cooper et al. (2007), the shot-record migration algorithm that was used for the 2D and 3D simulations incorporated weights prescribed by Bleistein et al. (2001). The formulation used by Bleistein et al. (2001) involves analysis of the Beylkin determinant (Beylkin, 1985) that describes the influence of the source-receiver geometry at a given image point. In a sense, the Beylkin determinant attempts to perform the transformation from continuous, infinite receivers on the surface to uniform illumination of a unit sphere surrounding each image point (Bleistein, 1987). However, the Bleistein migration formula is still an integral expression, corresponding to continuous sampling and no aperture limitations. When sampling is irregular and discrete, the integral is approximated by a sum and irregular illumination of the imaging hemisphere results. This process is analogous to calculating the integral of a function, $\int f(x)\,dx$, numerically by converting it to a sum, $\sum_{j} f(x_j)\Delta x_j$. The result of the sum will only approximate the true integral.

A first-order attempt is to just sample the function and add up the samples, such as $\sum_{j} f(x_j)$. If the samples were dense and regularly spaced (small, constant Δx) then the result of the sum will only be inaccurate by a scale factor, since Δx can be factored out of the sum. Sampling with a small, constant Δx is similar to the exhaustive dataset, with infinite aperture. However, if Δx is not constant, when samples are sparse and irregularly spaced in the case of a decimated dataset, $\sum_{j} f(x_j)$ will not be a good approximation of the integral. Weighting each sample in the sum appropriately, such as in $\sum_{j} f(x_j)\Delta x_j$, is required.

With this analogy in mind, our approach was that we require additional weighting factors in the summation or stacking process after migration, to be used in conjunction with the Bleistein weights applied during migration. The combination of the weighting schemes attempts to convert from discrete, irregular sampling to continuous, regular sampling. In the spirit of the Beylkin determinant, the weights should achieve uniform illumination of the imaging hemisphere. If we consider that the exhaustive survey represents ideal sampling, at least over a limited aperture, and that the Bleistein weights should convert that regular sampling on the surface to regular sampling on the imaging hemisphere, then our goal for a decimated survey is to weight traces to mimic the exhaustive survey. In particular, we can keep track of hit counts on the imaging

hemisphere and normalize by those hit counts. Industrial migration algorithms that are based on fold weights compensate for discrete, irregular sampling to some degree by performing a type of normalization, but in midpoint-offset coordinates. While angular illumination compensation is related to midpoint-offset weights, the two concepts are not the same, and moving from weighting in the surface acquisition domain to weighting in the image point domain may make the latter a more direct method for achieving normalization.

To accomplish the imaging hemisphere illumination compensation, we determine weights that are based on the angle delta. Delta describes the direction, which has both azimuth and dip components, of the vector that bisects the opening angle between the source-to-image-point ray and the receiver-to-image-point ray. Figure 6 shows the delta vectors for an image point and a source-receiver pair in 2D. For a flat reflector, the common-midpoint or Snell's Law reflections all have deltas of zero; therefore, a map of zero delta hit counts is the same as a common midpoint fold map. Like fold, zero delta hit counts are depth independent (discounting top-mute effects), but in general the non-zero delta distributions change with image point depth. The non-zero deltas extend the idea of fold to prestack data with non-Snell's Law raypaths, corresponding to diffractions. Even in the case of zero reflector dip, where the Snell's Law or zero delta reflections are most important, contributions from non-zero deltas are necessary in order to image lateral reflectivity contrasts.
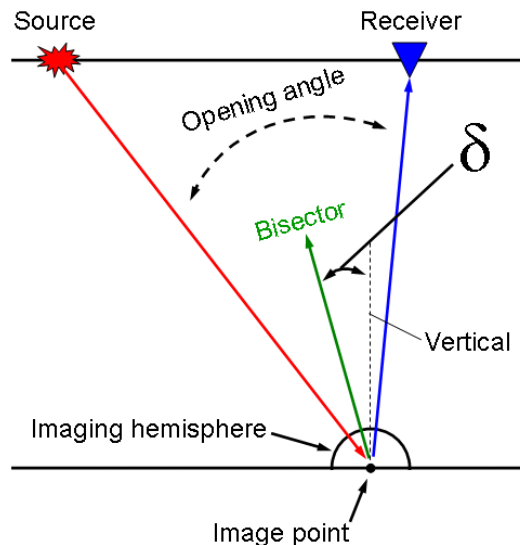

FIG. 6. Illustration of the angle delta, determined by the vector bisecting the opening angle between source and receiver rays. The positions of sources and receivers on the surface determine the distribution of delta angles on the imaging hemisphere. The theory of the Beylkin determinant requires equally weighted contributions to the image point from each delta.

When moving from the exhaustive survey to a decimated survey, the common midpoint fold decreases in a way related to the geometry of the decimation (Figure 7). This is not surprising, and neither is the idea that this change should be compensated for in prestack migration. The fold for non-zero deltas changes as well, but not in the same exact way as the zero deltas. The entire distribution of deltas changes in response to the

removal of sources and receivers. In order to achieve the same image point illumination with a decimated survey as was present with the exhaustive survey, the contributions of different deltas need to be weighted. We use two types of weighting schemes: fold weights that involve dividing by decimated dataset delta hit counts, and also ratio weights that involve the ratio of exhaustive to decimated delta hit counts. The concept of delta-dependent weights in prestack migration is not new; it has been used in the context of true-amplitude migration to compensate for irregular illumination of image points (e.g. Albertin et al., 1999, Audebert et al., 2003). In those cases, the approach consisted of a replacement of the Beylkin determinant in the prestack migration weights by delta hit count weights. Here we attempt to apply a similar concept to the case of footprint produced during prestack migration. However, we keep the Bleistein weights, including the Beylkin determinant therein, unchanged in the migration and multiply by additional delta hit count weights that are applied during stacking of imaged shot records after migration.
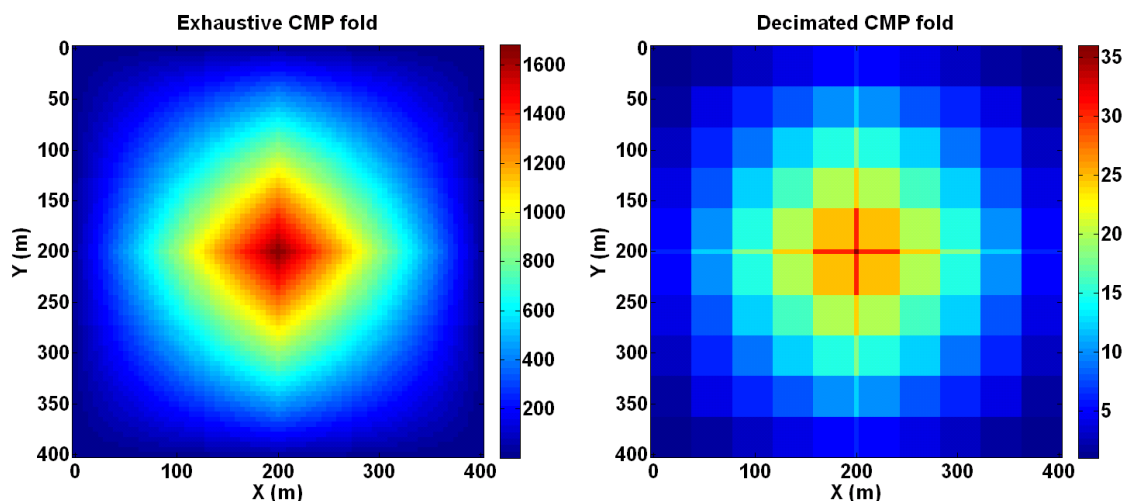

FIG. 7. Common midpoint fold for the exhaustive (left) and decimated (right) surveys from the 3D footprint simulation, as an example of delta hit count maps changing between exhaustive and decimated surveys, in this case for delta=0.

In a prestack migration, delta is directly related to dip of the migration impulse response; the delta vector is the normal to the migration impulse response (Figure 8). Delta is a function of source, receiver, and image point position, so every point on the impulse response for a given trace corresponds to a different delta, since the position of the image point is changing. Figure 8 shows a 2D impulse response divided into delta-limited bins. In our simulations of footprint, the steep dips of migration wavefronts do not cancel in the case of highly decimated datasets. This suggests that attempting to weight the different deltas on those migration wavefronts could have an impact on the footprint. In particular, down-weighting the large deltas could possibly reduce the presence of the artefacts.
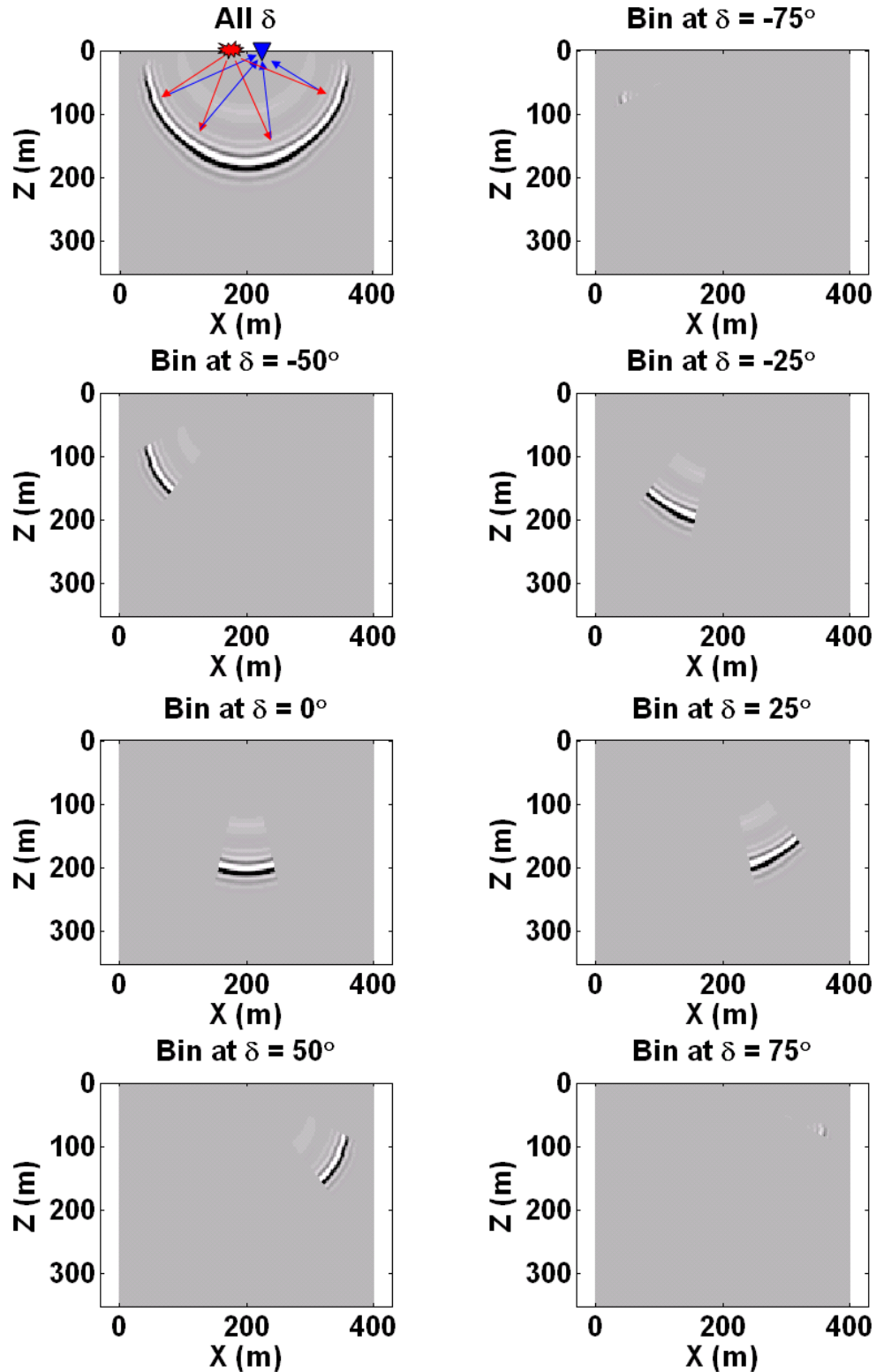
FIG. 8. Migration impulse response divided into individual delta angle contributions. Delta is determined by the opening angle bisector vector (refer to Figure 6), which is also the normal to the impulse response.

To implement the method, we first compute the delta distribution for each image point, for a set of predetermined delta bins. Computing these distributions requires ray tracing from all sources to all image points and from all receivers to all image points to find the bisector vector for each ray pair. Figure 9 shows the distributions for two image points from the 2D model, one in the middle of the model and one near the edge of the model, for the exhaustive survey and all five decimated surveys. Bins with a width of five degrees were used. Since the angles are determined by ray methods, binning of the delta angles appears to be necessary, otherwise the delta distributions of very closely spaced image points can be unrealistically different. However, the method for optimal binning has not yet been determined. Ray tracing to calculate the delta distributions does not constitute much of an additional computational burden, since the ray tracing step is already required in migration to compute traveltimes. In this example straight rays were used to compute the distributions. In practice, the delta computation step could be combined with the ray tracing step already being performed. As expected, Figure 9 shows that the image point in the middle of the survey displays a symmetric distribution of deltas, while the image point at the edge of the survey is dominated by deltas of only one sign. Figure 9 shows not only how the decimated surveys have fewer hits in each delta bin compared to the exhaustive survey, but also how the shape of the distribution changes as the decimation gets more extreme. Our weighting schemes attempt to compensate for this.
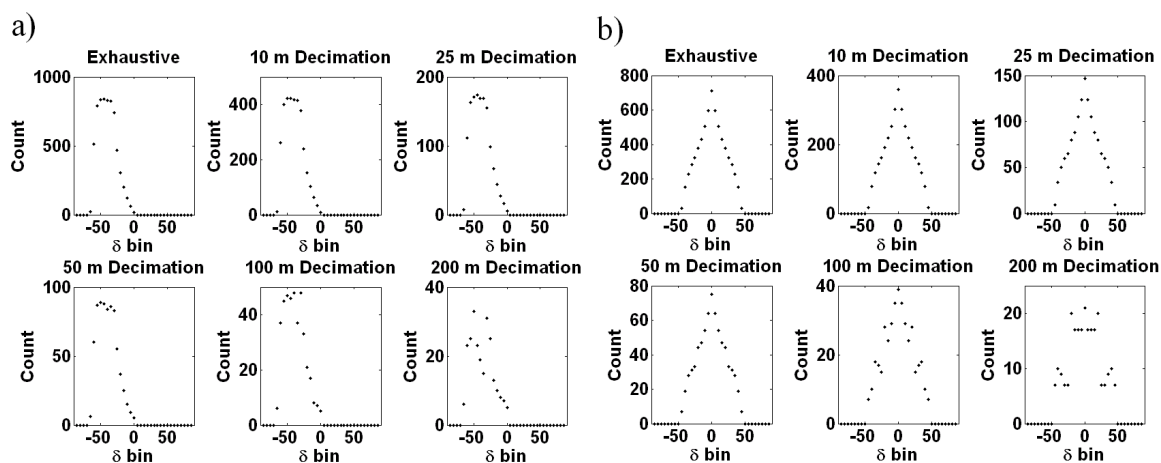

FIG. 9. Delta bin hit count distributions for two image points from the 2D model. Left (a) – image point at x=2.5 m, z=200 m, at the edge of the model. Right (b) – x=200 m, z=200 m, in the middle of the model. The six panels for each image point are the exhaustive dataset, and the 10 m, 25 m, 50 m, 100 m, and 200 m decimations.

The computation of delta distributions allows the weights for each delta-limited migrated trace contributing to that image point to be computed. We consider two possible weighting schemes: ratio weights and fold weights. For ratio weights the weight for a trace with a given delta is just the delta bin hit count in the exhaustive survey divided by the delta bin hit count in the decimated survey. Ratio weights attempt to convert the illumination of the decimated survey into that of the exhaustive survey, operating under the assumption that the Bleistein weights are designed (hence optimal) for exhaustive data with infinite aperture. For fold weights the weight is just one divided by the delta bin hit count in the decimated survey. Fold weights for the zero delta bin amount to just

the familiar division by common midpoint fold. Computation of fold weights only requires ray tracing for the shots and receivers in the decimated survey, while ratio weights involve ray tracing for the whole exhaustive survey, making them slightly more computationally intensive. Figure 10 shows both types of weights for the same two image points considered in Figure 9, again for the exhaustive survey and the decimated surveys. The ratio weights involve the exhaustive survey distribution in Figure 9 and dividing in turn by each decimated survey distribution. As expected, the ratio weights for the exhaustive survey are one for every bin, since in that case the weights are equal to the exhaustive hit count divided by itself. The weights for the decimated surveys change in response to the decimated hit counts changing, in a manner that attempts to compensate for the changing illumination. In general, the fold weights have higher weights associated with the larger delta angles, while the ratio weights have lower weights associated with large deltas. This suggests that the ratio weights may be more effective in reducing the presence of the step limbs of the residual migration wavefronts associated with footprint.
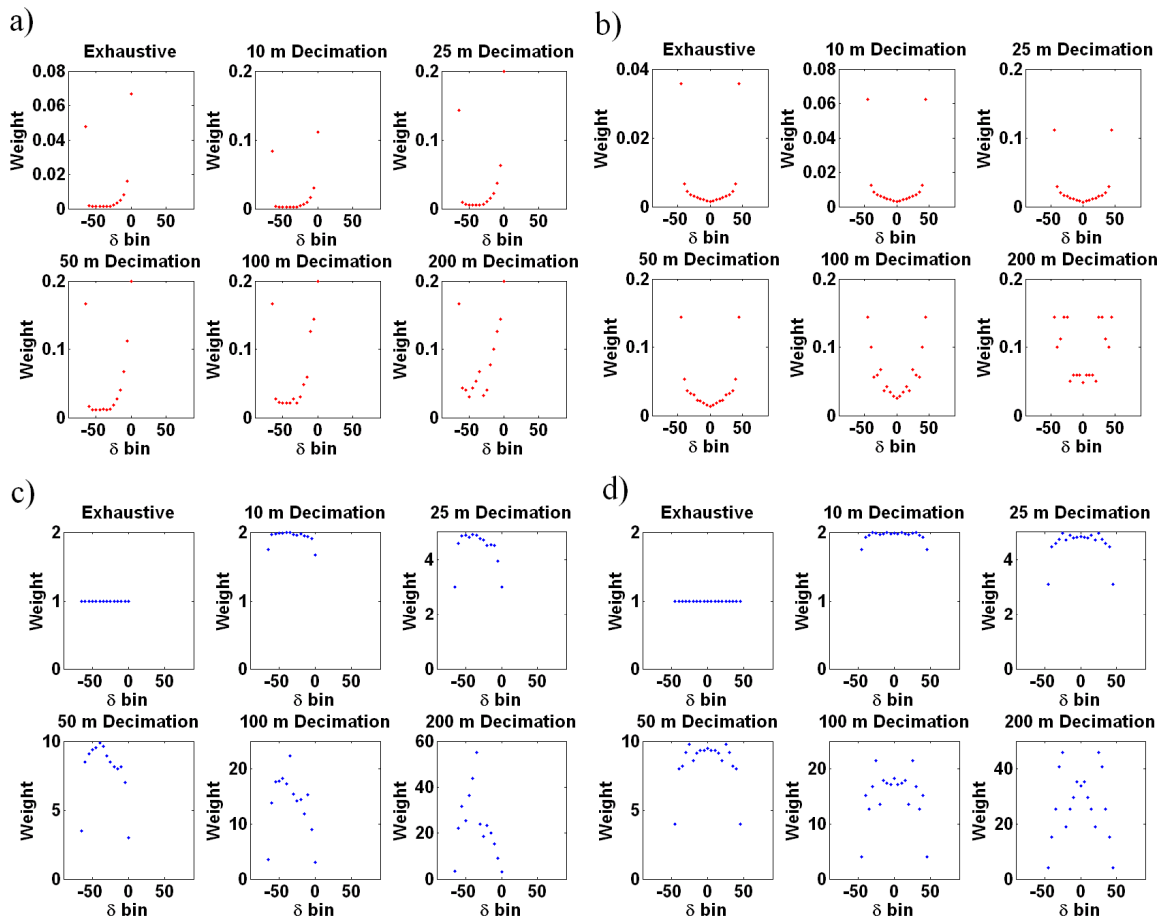

FIG. 10. Fold weights (a, b) and ratio weights (c, d) for the two image points from Figure 9 for the exhaustive and decimated surveys. Left (a, c) – image point at x=2.5 m, z=200 m, at the edge of the model. Right (b, d) – x=200 m, z=200 m, in the middle of the model. Fold weights appear to emphasize large deltas in the middle of the model, while ratio weights down-weight the large deltas. Ratio weights do nothing to the exhaustive survey.

In either the case of using fold weights or ratio weights, the weights are applied to each migrated trace getting stacked in for a particular image point. The process for a 3D shot-record migration can be described as follows. First, the jth shot record $\psi_j(x_r, y_r, t)$ is migrated, producing k delta-limited output volumes $\psi_j(x_i, y_i, z_i, \delta_k)$. Here, x_r and y_r are receiver coordinates, t is time, x_i, y_i, and z_i are the image point coordinates in the migrated volume, and δ_k indicates the kth delta bin. The delta hit counts are also computed for each image point; for the kth delta bin the hit count volume is $n(x_i, y_i, z_i, \delta_k)$. Then, the migrated shots are stacked to form the final image, and during the stacking process the weights are applied. This is described by

$$\text{Im}(x_i, y_i, z_i) = \sum_{j \, shots} \left[\sum_{k \, bins} W_k * \psi_j(x_i, y_i, z_i, \delta_k) \right],$$ (1)

where $\text{Im}(x_i, y_i, z_i)$ is the migrated image at the image point at (x_i, y_i, z_i) and W_k is the weight for the kth delta bin. In the case of fold weights, W_k is related to $n(x_i, y_i, z_i, \delta_k)$ by

$$W_k = \frac{1}{n(x_i, y_i, z_i, \delta_k)},$$ (2)

while in the case of ratio weights, W_k is related to $n(x_i, y_i, z_i, \delta_k)$ by

$$W_k = \frac{n_{exh}(x_i, y_i, z_i, \delta_k)}{n(x_i, y_i, z_i, \delta_k)}.$$ (3)

Here, $n_{exh}(x_i, y_i, z_i, \delta_k)$ is the hit count volume for the exhaustive survey.

To summarize the method, during migration a given trace contributes to all image points but generally with a different delta for each point. The position of the image point relative to the source and receiver locations determines the value of delta for each migrated trace. In this method, we apply a delta-dependent weight to each delta-limited migrated trace that contributes to an image point when the traces are stacked. In the simplest sense, this involves producing migrated delta-limited volumes, and then combining those volumes with volumes of weights that contain information about the delta hit counts for each image point in the volume. This produces a weighted migration. In reality, the step of outputting many migrated volumes is not necessary; the weights could be applied as traces are continually summed into the final image volume. While the weights are applied to individual shot records, the entire survey geometry is required to compute the weights. Our weights will also affect a common-image gather (CIG) because such a gather is usually constructed by simply not summing over sources.

2D EXAMPLE

To illustrate the application of the delta weighting scheme in 2D, we applied the technique to the same 2D footprint study shown in Figure 2. Figure 11 shows the results from prestack migration of the same six datasets, with delta ratio weights implemented when migrated traces were stacked together. Equal width delta bins of 5 degrees were used, with a bin centred on zero delta and bins distributed symmetrically for positive and negative deltas. The image from the exhaustive survey is identical in Figure 11 to what it was in Figure 2. This is because the ratio weights for the exhaustive dataset are just one for all delta angles, as shown in Figure 10. The images from the five decimated datasets have changed, though. The residual migration wavefronts that form the footprint artefacts in Figure 2 have become less pronounced in Figure 11. This is particularly apparent for the 50 m shot spacing in c) and the 100 m shot spacing in d). The image from the 200 m shot spacing shows a reduction of the wavefronts, but it does show some degree of horizontal striping, which is likely related to the binning of the delta angles. The images of the highly decimated datasets have not been improved to the point where they are identical to the image from the exhaustive dataset, but in our estimation they are an improvement over the same decimated surveys migrated without using the delta weights. Also, the image of the reverse polarity anomaly and the rest of the flat reflector have remained similar to the case without the delta weights, so the image of the target has not been degraded by application of this weighting scheme.

Figure 12 shows the same six prestack migrations using delta fold weights instead of delta ratio weights. Unlike in the case of delta ratio weights, the image of the exhaustive dataset using delta fold weights is not identical to the case where no delta weights were used (Figure 2). Figure 12 shows that the fold weights cause an enhancement of artefacts from the edge of the surveys. However, the fold weights have helped compensate for the limited aperture of the surveys. Amplitudes decay at the edges of the images in Figure 11, while the amplitudes remain more constant towards the edges in Figure 12. This benefit, though, came in association with the enhancement of edge artefacts. Possibly, these artefacts at the edges of the survey could be reduced by tapering before migration, in the same way that poststack migration edge artefacts are avoided. However, the wavefronts from the edges of the images do not appear to be the only wavefronts remaining in the images from the decimated datasets. The fold weights do not appear to reduce the presence of the wavefronts in the same way as the ratio weights do. Figure 12 also shows the same horizontal striping as was apparent in the most severe decimations in Figure 11. Figure 12 helps to show the connection between the horizontal stripes and the delta binning; the way in which the wavefronts from the edges of the survey are segmented is similar to the way the migration impulse response in Figure 8 was divided into delta bins. A different way of binning delta, as opposed to this boxcar method, may produce less of this type of horizontal striping. Figure 13 shows a detailed comparison between the prestack migrations without delta weights and with the two types of delta weights for the 50 m decimation and 100 m decimation.
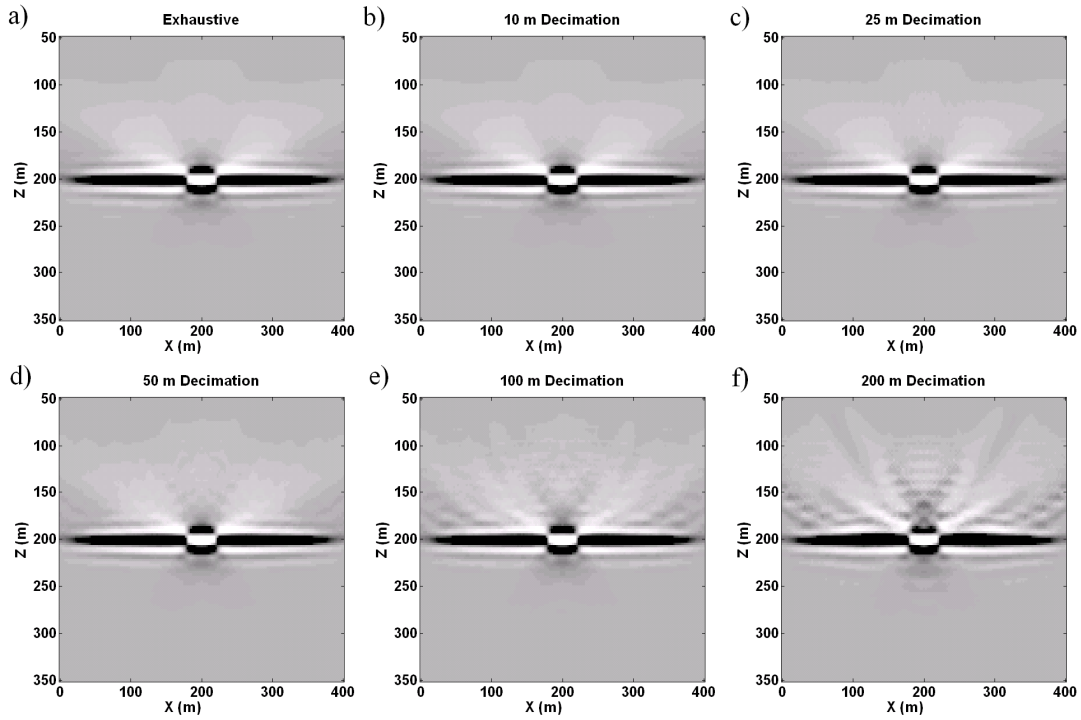
FIG. 11. Images produced from stacking migrated shot records from the exhaustive dataset and the five decimated datasets. Similar to Figure 2 except here delta angle ratio weights were applied when migrated traces were stacked. Compared to Figure 2, residual migration wavefronts are less pronounced.
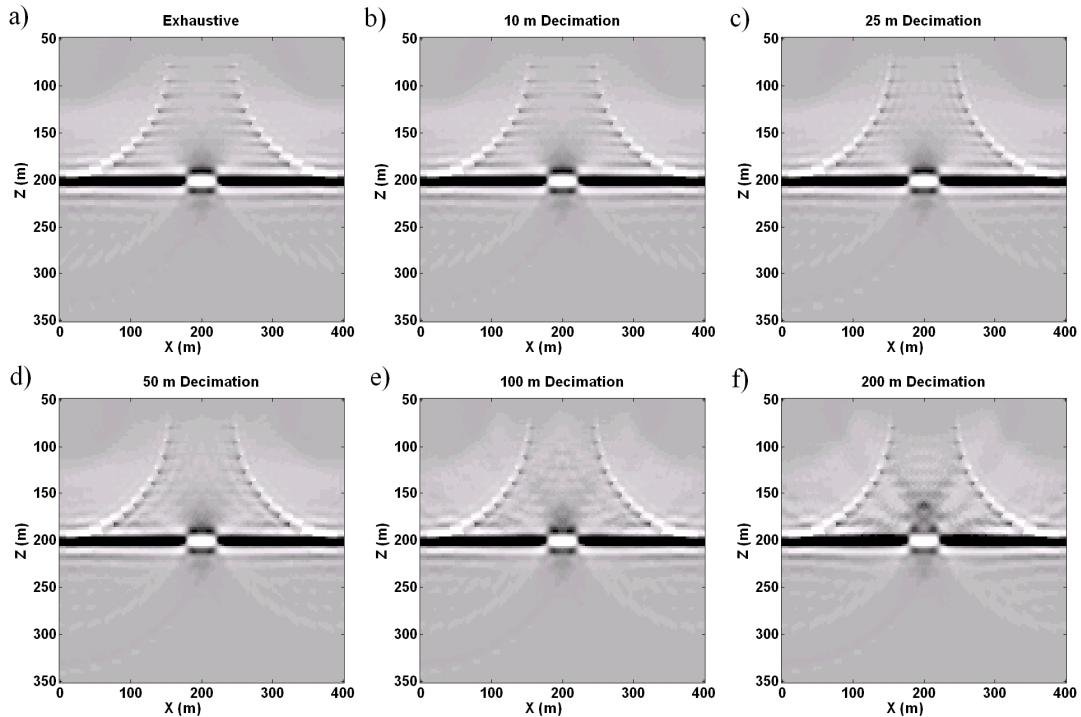

FIG. 12. Same as Figure 11 except delta fold weights were used instead of delta ratio weights. Fold weights do not appear to be as effective as ratio weights in reducing footprint, though they do compensate for limited aperture more effectively than the ratio weights.
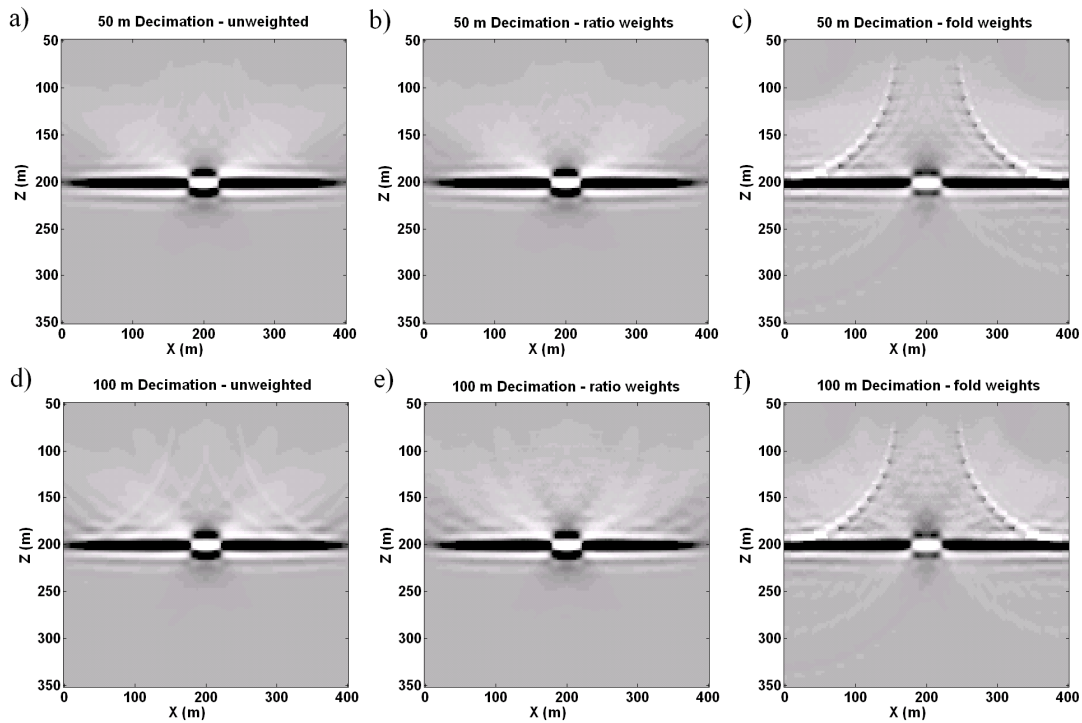
FIG. 13. Detailed comparison of images produced without delta weights (left), with delta ratio weights (middle), and with delta fold weights (right), for the 50 m decimated dataset (top row) and the 100 m decimated dataset (bottom row).

Since binning of delta angles is an integral part of the weighting method, we altered the bin width to assess the impact of this binning. In this 2D investigation, we did not explore bins with irregular widths; this will be the subject of future work. Figure 14 shows the results from using 1 degree bins for the delta ratio weights, compared to Figure 11 which involved using 5 degree bins. Figure 15 shows results using 15 degree bins. These figures suggest that the bin width does have a significant impact on the effectiveness of the delta ratio weights. Large bins do not seem to reduce the footprint artefacts as effectively, as they are not able to capture the detailed changes in hit counts as a function of delta angle. However, very small bins may make the weights too irregular with lateral position of the image point, resulting in some chatter in the image. This is especially apparent in the image of the 200 m decimated dataset using 1 degree bins. There may be a trade-off between amount of decimation and bin width. Highly decimated datasets may benefit from larger bins, while less decimated datasets may show the most improvement with smaller bins. Figure 15 also shows that the horizontal striping is indeed related to the delta binning, since on the image from the 200 m decimation the horizontal stripes are still noticeable but are at a larger separation than when the smaller delta bins were used. The 1 degree bins are so small that horizontal stripes do not seem to be present.
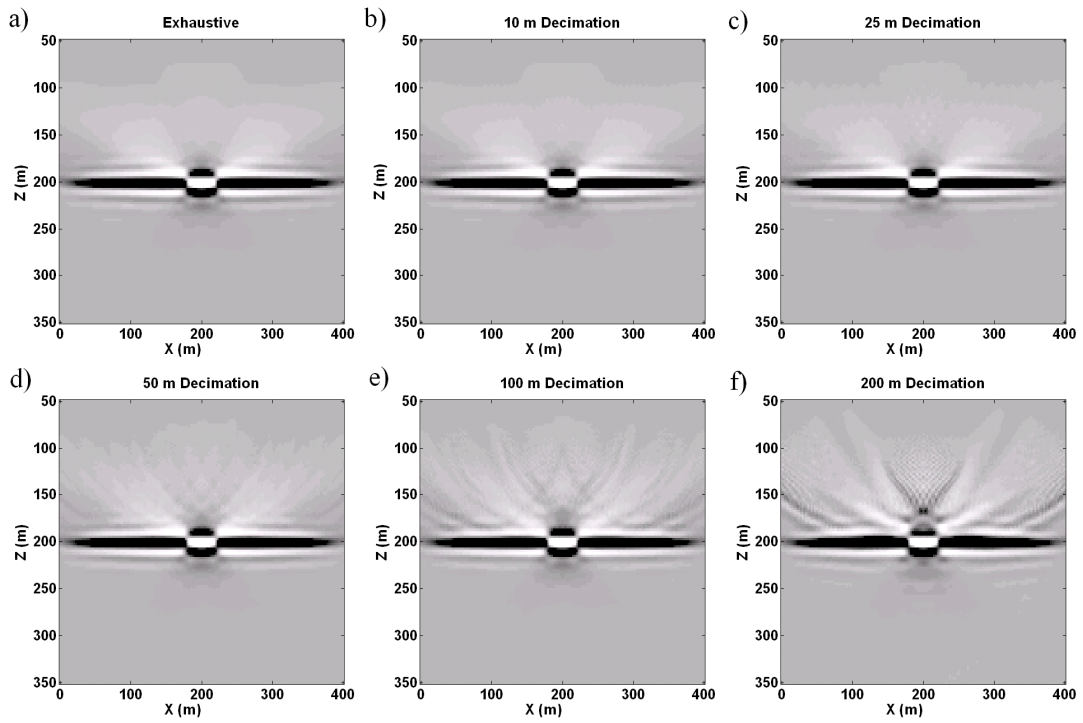
FIG. 14. Same as Figure 11 except 1 degree delta bins were used instead of 5 degree bins for calculating delta ratio weights.
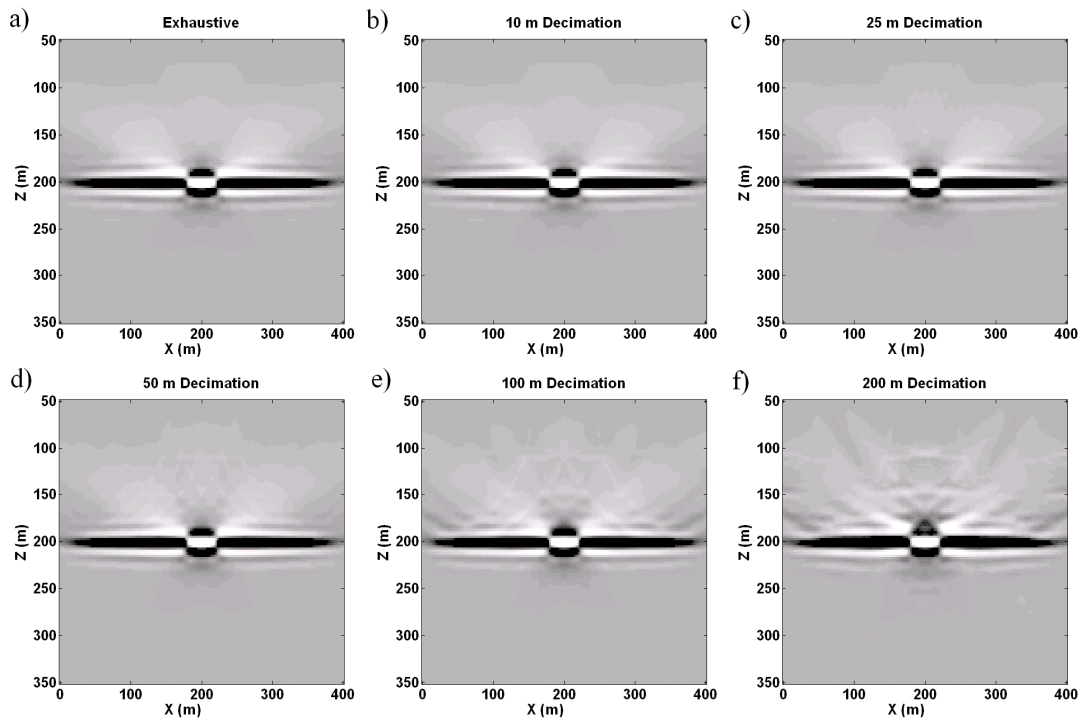

FIG. 15. Same as Figure 11 except 15 degree delta bins were used instead of 5 degree bins for calculating delta ratio weights.
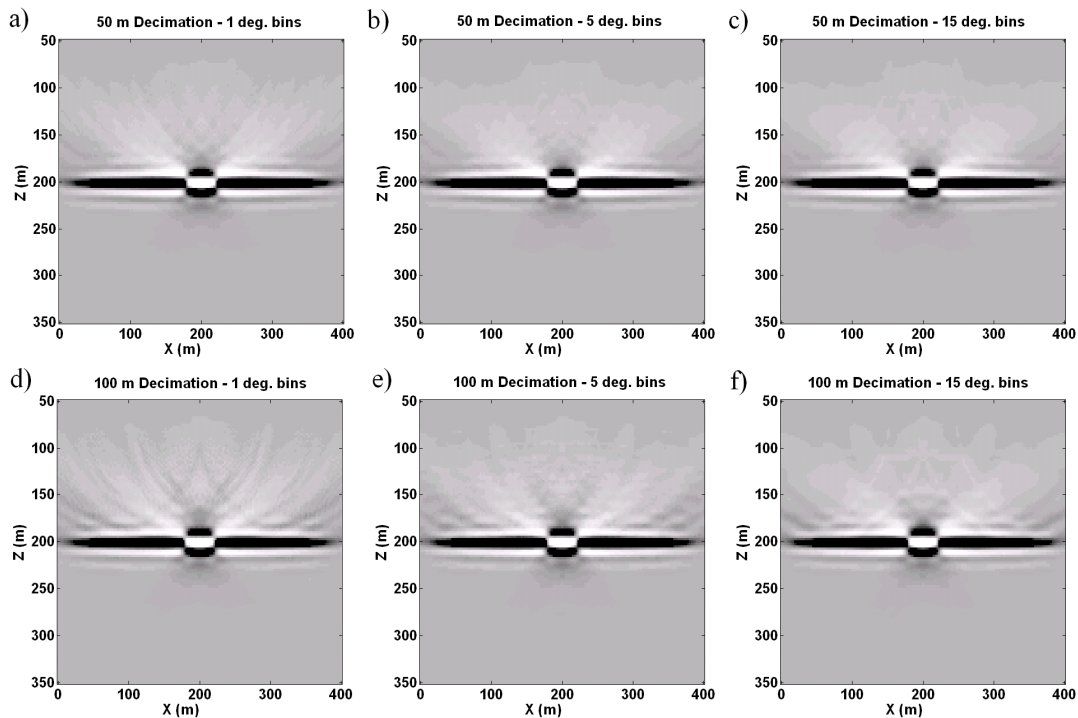
FIG. 16. Detailed comparison of using different delta bin widths for calculation of delta ratio weights for the 50 m decimated dataset (top row) and the 100 m decimated dataset (bottom row). The three different bin widths used were 1 degree (left), 5 degrees (middle), and 15 degrees (right).

As a last comparison using 2D delta weights, we show the effect of ignoring the azimuth of delta. In other words, binning of the absolute value of delta, instead of signed delta, is performed. Figure 17 shows the results of using the absolute value of delta for the delta ratio weight computations. While the residual migration wavefronts have been reduced slightly, they have not been reduced as much as when the sign of delta was considered (Figure 11). Figure 18 shows the detailed comparison between not using delta weights, and using both signed and unsigned delta weights. Not surprisingly, these results suggest that it is important to consider the sign (in 2D) or equivalently the azimuth (in 3D) of delta angles when implementing this type of illumination compensation.
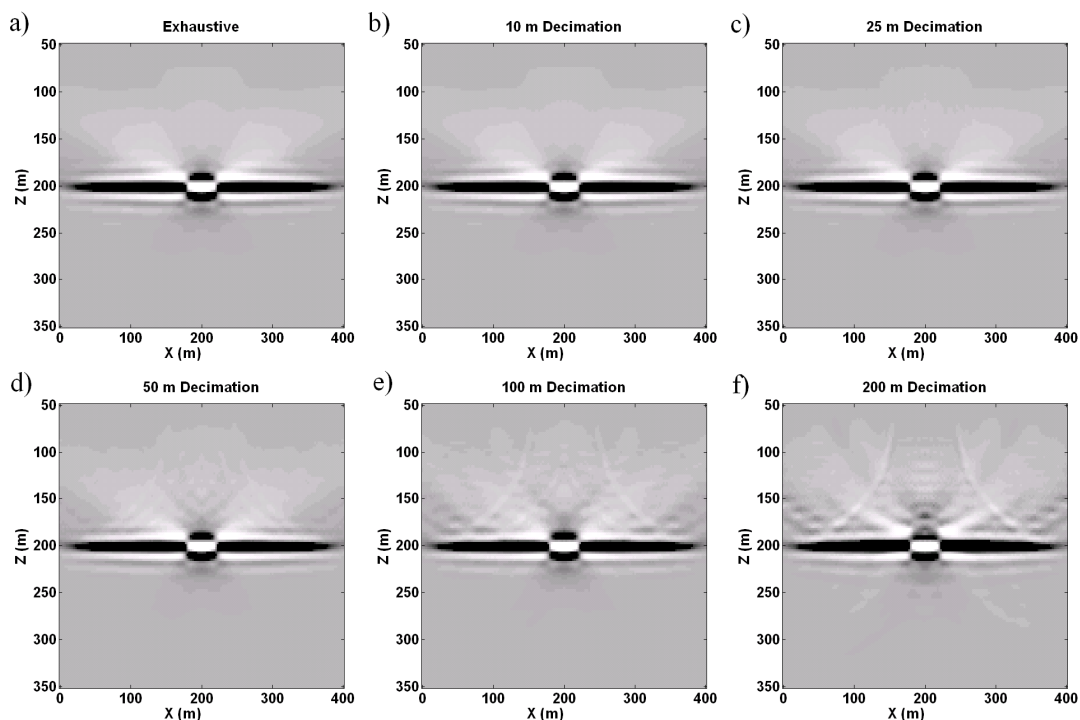
FIG. 17. Similar to Figure 11 except the absolute value of delta was used in binning instead of signed delta. This simulates not considering the azimuth of the delta angle when computing the delta ratio weights.
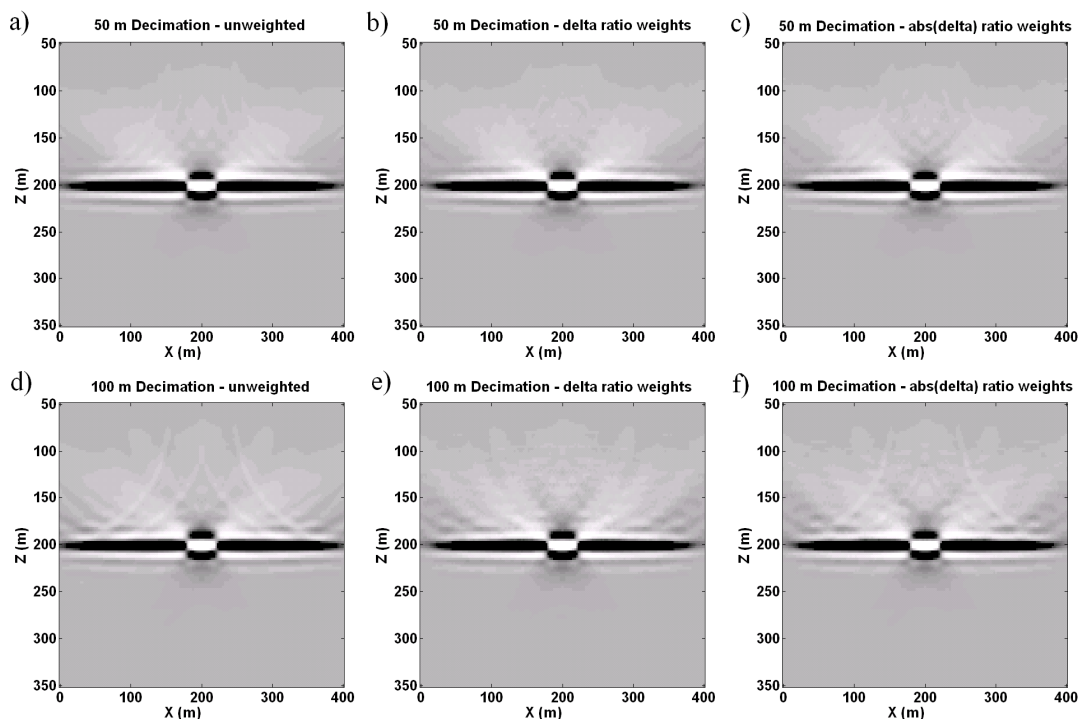

FIG. 18. Detailed comparison of images produced without delta weights (left), with signed delta ratio weights (middle), and with absolute value of delta ratio weights (right), for the 50 m decimated dataset (top row) and the 100 m decimated dataset (bottom row).

3D EXAMPLE

In a similar manner to the above 2D example, we are working on implementing the delta weighting scheme in 3D an applying it to the same 3D footprint model that was introduced earlier and presented in Cooper et al. (2007). The 3D case is slightly more difficult than the 2D case, particularly because the azimuth of the bisector vector must be considered. If azimuth is ignored, it is likely the same as working with the absolute value of delta in the 2D case. As shown above, the absolute value of delta was not as effective as using signed delta. This suggests that in 3D, consideration of azimuth is important. In 2D we find the dip angle by just taking a dot product of the bisector vector with a unit vector along the z axis. To find the azimuth in 3D we just take another dot product, this time with a unit vector pointing in the x axis direction. While we have yet to produce a full delta weighted prestack migration, here we will show some delta fold maps for shots from the exhaustive and decimated surveys to show how the weighting schemes would work. Figures 19 and 20 show the delta hit count maps for a shot at x=240 m, y = 400 m. The delta bins used were [0, 0.01), [0.01, 10), [10, 20), [20, 30), [30, 40), [40, 60), and [60, 90] degrees. We wanted a bin that was close to just containing zero delta to demonstrate that the zero delta hit count is the same as the common midpoint fold in the case of a flat reflector; this is shown in Figure 19. Azimuth was not considered in this binning example.
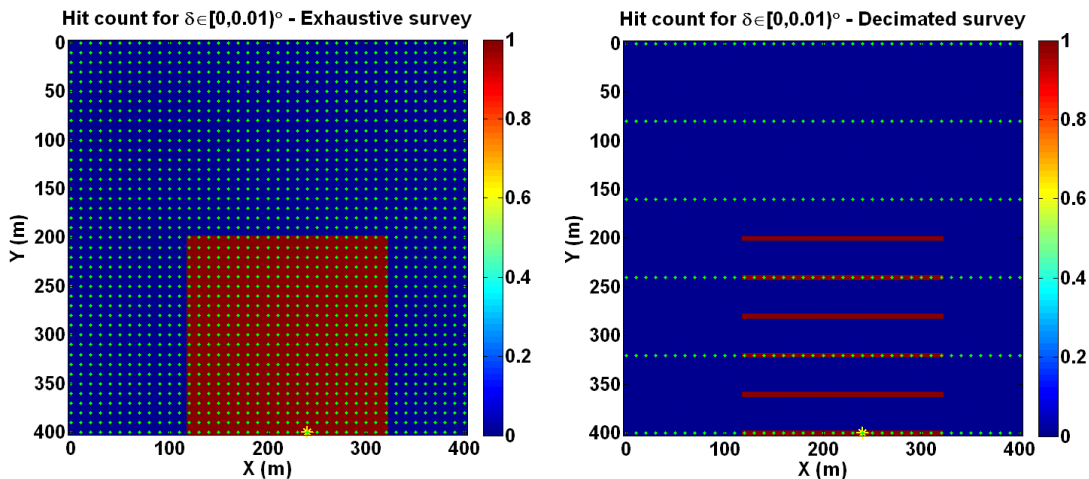

FIG. 19. Hit count maps for delta angles between 0 and 0.01 degrees for a shot located at x=240 m, y=400 m (position indicated by the yellow star), from the exhaustive dataset (left) and from the decimated dataset (right). Receiver locations for both datasets are indicated by green dots. These essentially zero delta hit count maps are identical to common midpoint fold maps for the shots.

Figure 20 shows the hit count maps for the other six delta bins, for the same shot from the exhaustive and decimated surveys. The delta weights used in prestack migration would come from the combination of similar hit count maps for all the shots in each survey. The delta hit count maps in Figure 20 are reminiscent of work done on illumination by Margrave (2005) in a study that attempted to reduce footprint by means of illumination compensation in phase-shift migration. This observation suggests that these delta weights are a type of illumination compensation applied to Kirchhoff shot-record migration. The delta hit count maps in Figures 19 and 20 show a lack of small

delta angles for image points between shot-receiver line midpoints in the decimated case. The delta ratio weights would attempt to compensate for this. Currently, we have the ability to compute the delta weights in 3D, and working code to migrate 3D shot records into delta bins. Soon we should have results from applying the weights to the migrated traces. More work is also ongoing with incorporating azimuth into the delta binning, and with examining different bin widths.
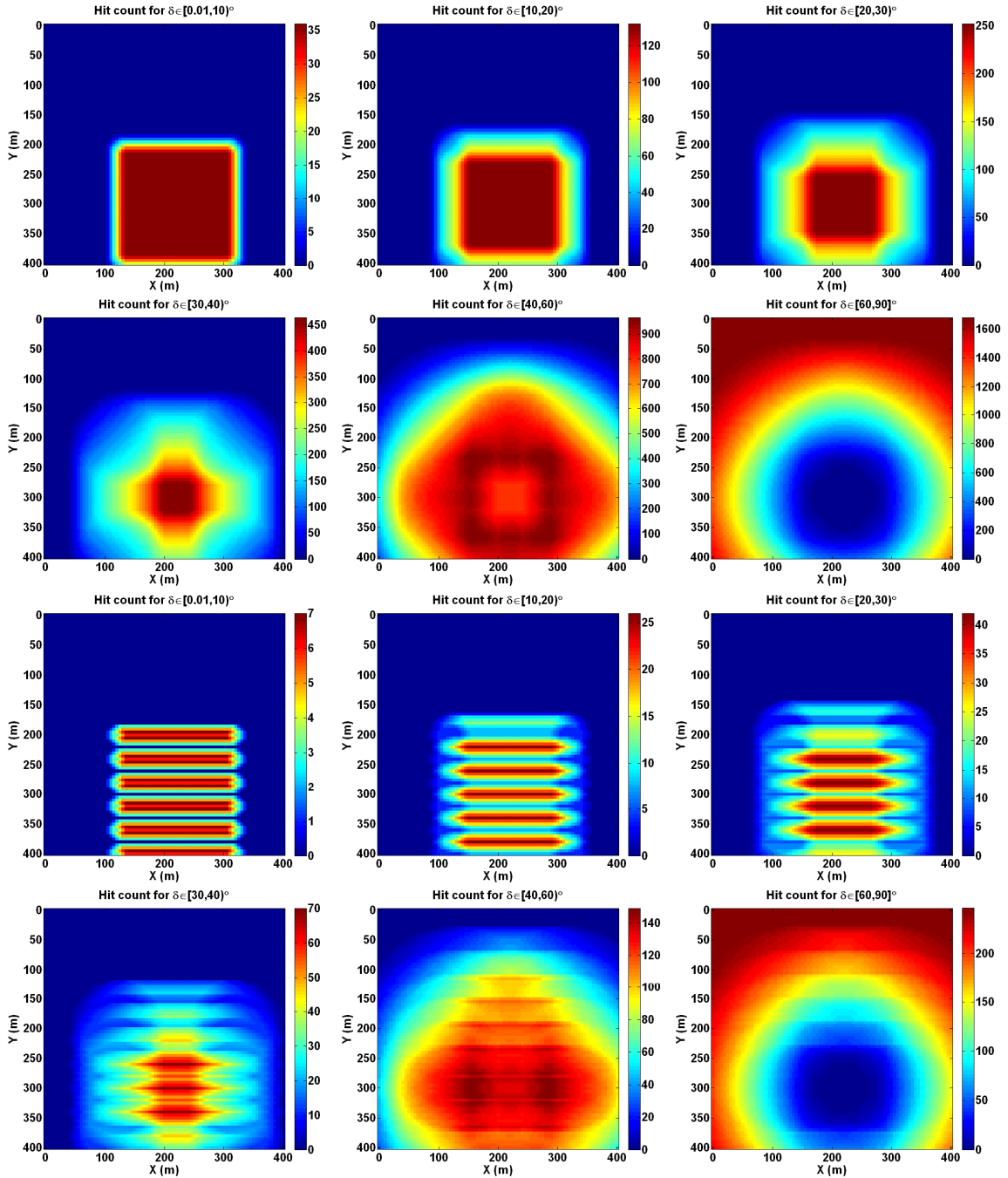

FIG. 20. Hit count maps for non-zero delta angles for a shot located at x=240 m, y=400 m, from the exhaustive dataset (top six panels) and from the decimated dataset (bottom six panels). The six delta bins were [0.01, 10), [10, 20), [20, 30), [30, 40), [40, 60), and [60, 90] degrees.

DISCUSSION AND CONCLUSIONS

Applying weights based on the distribution of raypath opening angle bisector directions to attempt to compensate for irregular image point illumination appears to reduce the presence of footprint produced when migrated shot records are stacked. The 2D simulation of decimated datasets show that the weighting scheme is not a substitute for proper sampling and cannot reproduce the quality of images produced from the exhaustive dataset, but the results do show that this type of compensation provides some benefit. The migrated sections incorporating delta ratio weights during stacking are an improvement over simple stacking of migrated shots, suggesting that more investigation is warranted.

An aspect that we have yet to investigate is the manifestation of footprint in common image gathers and whether this type of weighting would also show a benefit in that context. For now though, our aim is to produce a final image from stacking migrated traces that exhibits the least footprint. In our shot-record migration, this means that we are not focusing on producing the best migration of a single shot record, but the best stack of all migrated shots. Since the final image produced will result from stacking many migrated shots it makes sense that any weighting scheme used should have weights that depend on the distribution of shots as well as the distribution of receivers. Perhaps the apparent advantage of common-offset migration methods compared to a shot-record migration in our previous 3D simulations is related to this; common-offset migrations necessarily incorporate both source and receiver sampling because of the coordinate transform to midpoint and offset. However, if no partial stacking is being done before migration, it should not matter what type of gather is being migrated. Each migrated trace should be able to be weighted appropriately to get the most accurate amplitudes in the final image as possible. The delta weights for any migrated trace are a function of the distribution of all shots and receivers in the survey and are independent of whether the trace was in a shot record or in a common-offset gather.

We like the idea of these delta hit counts because the zero delta bin is the same as common midpoint fold for flat reflectors and the concept of dividing by fold when we do stacking is very well established. The non-zero delta hit counts extend the idea of fold to prestack data. We also like the fact that the ratio weights do nothing in the case of the exhaustive survey, since we consider the exhaustive survey to already have ideal sampling. However, we would like to see the weighting remove the strong aperture effect, which plagues even the exhaustive survey, and fold weights have the ability to do this, while ratio weights do not. Overall, in this simulation we think that the ratio weights perform better than pure fold weights. This may be related to the fact that we are combining the delta weights applied after migration with Bleistein weights that get applied during the migration. Possibly fold weights could perform better than shown here; perhaps the Bleistein weights should not be applied during the migration when using fold weights after migration. In an attempt to investigate this, we tried turning off all weights during the migration but retaining the fold weights or the ratio weights, which produced worse results than when the Bleistein weights were included. Probably, though, instead of turning off the migration weights completely, some type of weighting should still have been included in order to perform gain, etc.

As shown to some degree in the above 2D simulation, binning is an important factor in the method. The binning appears to be resulting in some horizontal striping in the images in some cases. It is possible that Gaussian windows in delta instead of boxcar windows would reduce this problem; this is currently under investigation. It is also unclear at this stage whether bins should be equal in size or not; in the 2D simulations the bins used were all regular in size, while the 3D delta hit count maps involved unequal bins. In 3D, consideration of azimuth is probably quite important, considering the 2D comparison between signed and unsigned delta. In 3D the choice of binning is even more complicated than in 2D because bins could be either on a polar grid or a rectangular grid; this is similar to the choice in binning offset in 3D into polar coordinates (offset and azimuth) or rectangular coordinates (inline offset and crossline offset). Despite all of the uncertainties that remain at this stage in our investigation, our purpose here was to present the idea behind the method and our results to date in 2D and 3D in order to solicit feedback. Further results in 3D are currently being produced.

ACKNOWLEDGEMENTS

REFERENCES

Albertin, U., H. Jaramillo, D. Yingst, R. Bloor, W. Chang, C. Beasley, and E. Mobley, 1999, Aspects of true amplitude migration: 69th Annual International Meeting, SEG, Expanded Abstracts.

Audebert, F., P. Froidevaux, L. Nicoletis, and H. Rakotoarisoa, 2003, Migration in the angle domain: an inside view: 65th Conference and Technical Exhibition, EAGE, Expanded Abstracts.

Beylkin, G., 1985, Imaging of discontinuities in the inverse scattering problem by inversion of a causal generalized Radon transform: Journal of Mathematical Physics, **26**, 99-108.

Bleistein, N., 1987, On the imaging of reflectors in the earth: Geophysics, **52**, 931-942.

Bleistein, N., J. K. Cohen, and J. W. Stockwell, Jr., 2001, Mathematics of Multidimensional Seismic Imaging, Migration, and Inversion: Springer.

Cary, P. W., 1999, Generalized sampling and "beyond Nyquist" imaging: CREWES Research Report, **11**, 42.1-42.23.

Cary, P., 2007a, 2-D Migration Footprint: CSEG Recorder, **32**, no. 6, 22-24.

Cary, P., 2007b, 2-D and 3-D Seismic Footprint: Presented at the 2007 Sensor Geophysical Technical Forum.

Cooper, J. K., G. F. Margrave, and D. C. Lawton, 2007, Simulations of seismic acquisition footprint: CREWES Research Report, **19**, 28.1-28.20.

Margrave, G. F., 2005, Footprint: A look at seismic acquisition geometries using prestack depth migration: CREWES Research Report, **17**, 9.1-9.42.